

# Prototype Tests for the CELESTE Solar Array Gamma-Ray Telescope

B. Giebels<sup>a,1</sup>, R. Bazer-Bachi<sup>b</sup>, H. Bergeret<sup>d</sup>, A. Cordier<sup>d</sup>,  
G. Debiais<sup>f</sup>, M. De Naurois<sup>c</sup>, J.P. Dezalay<sup>b</sup>, D. Dumora<sup>a</sup>,  
P. Eschstruth<sup>d</sup>, P. Espigat<sup>e</sup>, B. Fabre<sup>f</sup>, P. Fleury<sup>c</sup>,  
C. Ghesquière<sup>e</sup>, N. Herault<sup>d</sup>, I. Malet<sup>b</sup>, B. Merkel<sup>d</sup>,  
C. Meynadier<sup>f</sup>, M. Palatka<sup>g</sup>, E. Paré<sup>c</sup>, J. Procureur<sup>a</sup>,  
M. Punch<sup>e</sup>, J. Québert<sup>a</sup>, K. Ragan<sup>a,2</sup>, L. Rob<sup>h</sup>, P. Schovanek<sup>g</sup>,  
D.A. Smith<sup>a</sup>, J. Vrana<sup>c,3</sup>

<sup>a</sup>*CEN de Bordeaux-Gradignan, Le Haut Vigneau, F-33175*

<sup>b</sup>*CESR, Toulouse, F-31029*

<sup>c</sup>*LPNHE, Ecole Polytechnique, Palaiseau, F-91128*

<sup>d</sup>*LAL, Université Paris Sud and IN2P3/CNRS, Orsay, F-91405*

<sup>e</sup>*LPC, Collège de France, Paris, F-75231*

<sup>f</sup>*GPF, Université de Perpignan, F-66860*

<sup>g</sup>*Joint Laboratory of Optics of PU and Inst. of Physics AS CR.*

<sup>h</sup>*Nuclear Centre, Charles University, Prague, CR.*

---

## Abstract

The CELESTE experiment will be an Atmospheric Cherenkov detector designed to bridge the gap in energy sensitivity between current satellite and ground-based gamma-ray telescopes, 20 to 300 GeV. We present test results made at the former solar power plant, Themis, in the French Pyrenees. The tests confirm the viability of using a central tower heliostat array for Cherenkov wavefront sampling.

---

<sup>1</sup> e-mail: [giebels@cenbg.in2p3.fr](mailto:giebels@cenbg.in2p3.fr)

<sup>2</sup> Visiting from McGill University, Montreal, Canada.

<sup>3</sup> Deceased.

# 1 INTRODUCTION

The CELESTE experiment uses the Electricité de France central receiver solar power plant at Themis (N. 42.50°, E. 1.97°, 1650 m. a.s.l.) as a gamma-ray telescope [1]. The project is fully funded and will begin observations in early 1998 with 18 heliostats, growing to 40 in the following year. Figure 1 sketches the principal of the CELESTE approach. This paper describes test results accumulated during the design and construction phase. Emphasis is placed on Cherenkov measurements made using six heliostats between October 1996 and February 1997.

## 1.1 Science

Active Galactic Nuclei (AGNs), pulsars, and supernova remnants are complex “cosmic accelerators”. High energy radiation dominates the power output of certain classes of these objects [2,3]. Study of their high energy spectra provides insight into the origin of cosmic rays, especially at the highest energies, and the nature of AGNs.

Photons from distant galaxies also probe the extragalactic medium: gamma-rays incident on near infrared photons are above threshold for  $e^+e^-$  pair production and are thus absorbed, with approximately one attenuation length for GeV to TeV photons traversing cosmological distances. In this way gamma-ray spectra provide information on galaxy formation and, indirectly, on the nature of dark matter [4].

Around 1990 two breakthroughs revolutionized the field. First, ground-based atmospheric Cherenkov detectors became sensitive, reliable instruments above a few hundred GeV, led by the Whipple imager [6] and followed by the Themistocle and ASGAT wavefront samplers at Themis [7,8]. Recent measurements by CAT and other imagers of flaring in Mrk 501 underscore the rapid improvement of ground-based detectors [9]. Second, the EGRET instrument on the Compton satellite measured the spectra of over 150 point sources and mapped the galactic diffuse gamma-ray emission, in the energy range  $0.1 < E_\gamma < 10$  GeV [10]. The energy range currently inaccessible either by satellite or ground-based detectors,  $20 < E_\gamma < 200$  GeV, is particularly rich with information on the acceleration and absorption processes. Bridging this energy gap is a key scientific goal.

## 1.2 Solar Arrays as Atmospheric Cherenkov Detectors

The Atmospheric Cherenkov Technique has been described extensively elsewhere: see for example [5–9]. A few points bear repeating.

The minimum energy threshold of a Cherenkov telescope is limited by accidental trigger coincidences induced by photons from the night sky. For a constant diffuse night sky light  $\phi$  (photons per unit time, area, and solid angle), and a coincidence time gate  $\tau$  the threshold scales as

$$E_{threshold} \propto \sqrt{\frac{\Omega\tau\phi}{A\epsilon}} \quad (1)$$

where  $\Omega$  is the solid angle seen by a phototube and  $\epsilon$  is the photon collection efficiency. Current telescopes have pushed  $\tau$  and  $\Omega$  to their practical limits. Until technological progress improves quantum efficiencies and hence  $\epsilon$ , lower energy thresholds require larger mirror areas,  $A$ .

Solar heliostat arrays offer the advantage of a large mirror area available without additional construction costs. The optical configuration is similar to that of multiple mirror wavefront samplers such as Themistocle. The main difference is the common focus of all heliostats is situated at the top of the tower. Secondary optics disentangle the light coming from each of the heliostats, as sketched in figure 1. The STACEE collaboration is building a similar detector in the United States [12].

Imagers are superior to samplers above 200 GeV, since the fine sampling of their cameras allows excellent hadron rejection. But below 100 GeV, hadron backgrounds are naturally suppressed because the Cherenkov yield of the hadron showers decreases faster than that of the gamma showers. Hence, the advantage of the imagers in this regard is less.

At low energies, the background due to cosmic ray electrons is greater than above 200 GeV due to an energy spectrum steeper than for hadrons. Since electron induced showers are practically indistinguishable from gamma-ray showers, angular resolution is the key to suppressing the electron background. But angular resolution, especially at lower energies, tends to be limited by shower development rather than by instrument response. Scattering in the first few generations of the shower and deflection of low energy secondaries in the geomagnetic field are the factors limiting angular precision. Hence, a high-granularity imager does not necessarily outperform a wavefront sampler. Both should achieve angular resolutions around  $0.1^\circ$ .

Sections 2 and 3 describe the apparatus and the main results of the prototype

tests. Based on these results we compare sampling arrays and imagers for the low energy domain in section 4.

## 2 EXPERIMENTAL APPARATUS

We chose two well-separated (156 m) groups of three nearby (20 m) heliostats each to test the strategy adopted for CELESTE: a long lever-arm for event reconstruction combined with short path-length differences within subgroups to simplify the trigger electronics (figure 1).

### 2.1 Photomultiplier tubes

The Philips XP2020 used for these tests is a fast 12-stage 2-inch photomultiplier that has been used extensively at the Themis site. The photocathode is bialkali and overall it is very similar to the 8-stage XP2282B we have selected for the 40-heliostat experiment. The bases were of the “C” type, supplied by Philips. We measured their gain via the single photoelectron peak in both charge and voltage (see [13] for a discussion). All gains were measured with 15 meter RG-58 cables as were used for the experiment. The average gain was  $10^6$  and anode currents due to night sky light were typically  $70 \mu\text{A}$ . The phototube signals were amplified by 10 using a LeCroy 612AM NIM module.

### 2.2 Readout

Electronics and computers were installed in a counting house just beneath the secondary optics. For the tests we used three Struck DL515 Flash ADC’s. The DL515 has four channels that each sample at 250 MHz. Interleaving a signal over four channels provides 1 ns sampling. These VME modules were controlled by a Motorola 68040 processor running under the Lynx operating system. We recorded 400 one-nanosecond 8-bit voltage samples from each Flash ADC for each trigger. Trigger rates were under 10 Hz and deadtime due to readout was less than 5%.

A typical Cherenkov event is shown in figure 3. As only three Flash ADC’s were available at that time we recorded the six phototube signals by AC-coupling the analog sum of three phototubes to a single Flash ADC, as sketched in figure 4. This increased the night sky light in the data. Short delays (8 and 16 ns) were added to separate Cherenkov pulses from each another. The average overall conversion factor was  $1.8\gamma e$  per digital count, with a  $\pm 15\%$  channel-to-channel variation. (The full-scale detector will have a conversion factor of

0.4 $\gamma e$  per count to enhance sensitivity to small pulse heights.) The electronic pedestal was negligible. With AC-coupling, the pedestal of the night sky light fluctuations was  $1.2 \pm 1.0\gamma e$  per 10 ns. We studied the precision of the time and charge measurements made with the FADC's by superimposing simulated phototube pulses onto real night sky data and then reconstructing the pulses. For an amplitude of 3 photoelectrons we found  $\delta(\Delta t) \simeq 0.5$  ns and  $\delta V/V \simeq 15\%$ . The precision improves with increasing pulseheight.

In addition to the VME system, we also used Camac ADC's (LeCroy 2249SG), TDC's (LeCroy 2228A), discriminators (Phillips 7106), and scalers (LeCroy 2551) with PC/GPIB readout for each phototube. These provided cross-checks of the Flash ADC results.

### 2.3 Trigger

#### *Digital trigger:*

For each phototube an amplifier output was DC-coupled to a discriminator circuit with a 20 ns output gate. A multiplicity requirement (*e.g.*, five of the six channels above threshold) stopped the Flash ADC's and prompted the acquisition computer to read the Flash ADC memories.

Threshold settings were the same for all six phototubes. The DC-coupling causes a baseline voltage  $V_{sky}(b) = bgeR$  that varies with the night sky light induced rate of  $b$  photoelectrons per nanosecond at the photocathode, where  $g$  is the combined phototube and amplifier gain,  $R = 50\Omega$  is the termination resistance, and  $e$  is the electron charge. We made frequent measurements of the unamplified anode current which we used when converting the trigger thresholds to photoelectrons. A typical value of  $V_{sky}$  was -30 mV. The discriminator thresholds were -80 mV, which corresponds to 5 photoelectrons above the mean night sky light level (except as noted).

#### *Hybrid Analog-Digital trigger:*

Atmospheric Cherenkov telescopes operate at trigger thresholds limited by accidental triggers due to night sky light. For the CELESTE experiment the rate of single photoelectrons on an individual phototube is high (600 MHz), and a goal of the full 40-heliostat experiment is to lower the effective trigger threshold to 3 photoelectrons on each phototube, corresponding to gamma-rays of about 20 GeV.

The analog trigger sums the signals from the phototubes within a group of heliostats, and the sum is discriminated, as sketched in figure 2. The fast time structure of the phototube pulse and the synchronous secondary optics provide

the smallest possible  $\tau$  (eq. 1), and thereby a low energy threshold. A purely analog scheme generates triggers which arise from, for example, phototube afterpulses, charged particles or muons. A coincidence of the discriminated outputs from groups eliminates noise triggers which would occur using only analog sums. This coincidence between analog sums is the hybrid analog-digital trigger. The principal reason that CELESTE will use a hybrid analog-digital trigger is that it lowers the trigger threshold at which the rate due to Cherenkov flashes dominates the rate due to accidental coincidences of night sky light induced pulses. This allows operation nearer the effective 3 photoelectron per heliostat threshold, which should achieve a 20 GeV gamma-ray threshold.

Two three-channel analog summing circuits, illustrated in figure 2, were available during the February '97 tests, which we used for the measurements described in section 3.2. The key component is a passive inductive summer/splitter manufactured for satellite radio-frequency repeaters [11]. The bandpass is 500 MHz and the insertion loss is 5.6 dB.

#### 2.4 Heliostats

Figure 5 shows a single heliostat. The microprocessor that controls the two DC motors of the alt-azimuth mount receives pointing instructions from a central computer via a serial bus. The motor step size is 0.14 mr. Heliostat alignments were adjusted by maximizing the phototube anode current during star tracking, and were cross-checked using stars at widely spaced points in the sky. The spherical mirrors are silver back-coated with a surface area of 54 m<sup>2</sup>.

#### 2.5 Secondary optics

We aluminized two searchlight mirrors and mounted them in the tower in the space formerly occupied by the solar heat receiver. Each pointed towards a group of heliostats. The mirrors are f/0.4 parabolas with an 150 cm aperture and 90% reflectivity. The field-of-view (“fov”) is thus in principle given by the angle subtended by the secondary mirror when viewed from a heliostat. The heliostats we used are all approximately at 140 meters from the tower so our fov was  $1.5/140 = 11$  mr (full width). However, the short focal length gives rise to large off-axis aberrations so that light falling near the mirror edge is lost.

We calculate the light collection efficiency by ray-tracing techniques, up to the phototubes. We modeled the detailed heliostat structure, and used the

phototube positions in the parabola's focal plane that were used during the experiment. Various measurements confirm the validity of our calculations.

*Star drift scans:* We made two dimensional maps of the heliostat optical acceptance by letting stars drift through the field of view and recording a photomultiplier's anode current. (Phototube high voltage was reduced to avoid excessive anode current.) Figure 6 shows one such scan. Superimposed is the ray tracing result, normalized to the peak anode current. We see that the effective *fov* is 7.5 mr (FWHM) for a point source.

*Night sky light:* We measured the night sky light  $\phi$  (see equation 1) with an XP2020 phototube in a collimating cylinder whose field-of-view was defined by diaphragms. This was done in order to make a *direct* measurement of the night sky with a well-defined *fov* and with a flat acceptance over the entire *fov*. This also avoided other noise such as albedo. The night sky intensity at zenith was found to be

$$\phi = (300 \pm 45)\gamma_e/m^2 \text{ sr ns.}$$

If we assume a flat spectrum from 310 to 650nm we can deconvolute the intensity from the phototube quantum efficiency and obtain a value of

$$\phi = (1.8 \pm 0.3) \cdot 10^{12} \text{ photons}/m^2 \text{ sr s}$$

which is comparable to measurements at other dark sites[12,13]. We also measured the light from the same part of the sky after reflection by a piece of heliostat mirror. The intensity decreased by 20%, in good agreement with the measured heliostat wavelength dependent reflectivity.

Using ray tracing programs to calculate the overall transmission of our optics, the above measurement leads us to expect a photocathode illumination of  $b = 0.43\gamma_e/\text{ns}$  for no albedo. If we assume albedo due to 20% ground reflectivity,  $b$  increases to  $0.57\gamma_e/\text{ns}$ . The measured values were typically  $b = 0.5$ , with  $\pm 5\%$  variation from night to night. After a heavy snowfall in January, the measured illumination doubled. We reproduce this effect by assuming 90% ground reflectivity. The definitive secondary optics now being installed is less sensitive to ground albedo.

*Laser data:* The Themistocle [7] laser illuminates the heliostat field with 4 ns pulses (rms) at  $\lambda = 330 \text{ nm}$  via a diffuser placed five meters below the parabolic secondary that observes the Eastern group of three heliostats. We recorded 10,000 laser pulses with the Flash ADC's and the six phototubes, and we compared the laser intensity with the results obtained from Themistocle, corrected for the different detector geometries. We obtain the same average laser intensity as they, thereby validating our optics calculations for a source in the mirror focal plane, a test complementary to the study of a star (point

source at infinity) or the night sky (diffuse source).

## 2.6 Monte Carlo shower and detector simulations

The measurements described in the next section are compared to the results of a Monte Carlo simulation. We generated 650,000 proton air showers with ISU [14], with energy  $E_p > 150$  GeV according to a power law energy spectrum of the form

$$\phi_P(E) = 2.43 \left( \frac{E}{\text{GeV}} \right)^{-2.78} / (\text{cm}^2 \text{ sr GeV}) \quad (2)$$

over a disk of radius 300 meters centered at D2 and uniformly within  $2^\circ$  of zenith [16]. In addition we simulated 60,000 helium showers using the spectrum from the same reference, and 100,000 lithium showers according to the measurements of [17]. (As can be seen in figure 10 the contribution from lithium is small and so we have neglected the heavier nuclei.) Cherenkov photons reaching the heliostats are then propagated through a detector simulation that includes the optical and phototube properties, allowing us to calculate the expected trigger rates as well as the charge and time distributions.

In addition to the ISU work, we have performed complete simulations using the CORSIKA shower generator [15], and found reasonable agreement between the two Monte Carlos. All simulation results shown in this paper are from ISU (with the exception of figure 8).

## 3 STUDY OF AIR SHOWERS WITH A SIX-HELIOSTAT ARRAY

We took data during the December, January, and February 1996-1997 new moon periods. The results presented in this article use the February data, recorded with the Flash ADC's. The trigger multiplicity was 5 heliostats out of 6 above threshold and the single PM threshold was 5 photoelectrons. To estimate the charge in an event (figure 3) we sum 4 samples before the peak and 11 samples after the peak. The pulse arrival time on a single channel is taken as the voltage-weighted mean over the same samples. The selection cuts we use in the analysis are a requirement of a minimum peak height of four Flash ADC counts for five out of the six channels corresponding to 7 photoelectrons, without pedestal subtraction.

A variety of evidence convinces us that our data is dominated by Cherenkov light pulses from extended air showers. For example, figure 7 shows a strong



correlation between the pulseheights observed in heliostats F5 and F11. Accidental coincidences between random phototube noise (*e.g.* night sky or afterpulses) would be uncorrelated. Similarly, the timing correlation within the 20 ns coincidence gate (shown in figure 9), the “break” in the coincidence rate curve near 5 photoelectrons (figure 11) and the good agreement between the observed and predicted differential charge distributions (figure 13) provide further evidence. We will discuss these arguments in the following sections.

*Convergent pointing:* Equation 1 underscores the necessity of a small field-of-view in order to achieve a low energy threshold. A consequence of a small *fov* is that widely-spaced heliostats aimed at a gamma-ray source will in general *not* all see Cherenkov photons from a given atmospheric cascade. Stated differently, to optimize photon collection efficiency the heliostats must track the zone in the atmosphere where the Cherenkov light is generated. In the tests all heliostats were pointed at a point  $z$  kilometers above heliostat D2 (see figure 1). We varied  $z$  from 3 to 100 km.

### 3.1 Timing measurements

Figure 8 shows the distribution of the differences of the arrival times averaged over the F and the D heliostats. The top plot shows measurements made with the Flash ADC’s, while the bottom plot was made using the CORSIKA Monte Carlo. The width is due mainly to the thickness of the Cherenkov wavefront for hadron showers: the dispersion due to the zone defined by the overlap of the fields of view of the two groups of heliostats is of the order of 3 nanoseconds. The 0.4 ns difference between the measured and calculated mean times are due in part to accumulated uncertainties in the cable delay measurements, as well as to a small uncertainty in the heliostat pointing arising from the method we used to place the phototube in the secondary mirror focal plane.

Figure 9 summarizes the measurements of the arrival time difference for Cherenkov light as a function of pointing altitude. The points are the means of the distributions of the differences between the arrival time for each heliostat and the arrival time for F11.

The curves plotted on the figure come from a simple model, where we assume that the light is emitted from the point that the heliostats aim at, and the time difference is then

$$c\Delta T_i = \sqrt{z^2 + d_i^2} - z, \quad (3)$$

where  $d_i$  is the distance between heliostat  $i$  and F11. This particular heliostat, the farthest from the observed sector in the sky, was chosen to give positive

time differences in figure 9. We imposed agreement between the simple model and the data at 99 km, to correct for the 0.4 ns offset described in the preceding paragraph. The good agreement between the data and the simple model demonstrates the ability to point the telescope accurately and to measure nanosecond time differences accurately, which are two critical aspects of the performance of a Cherenkov gamma-ray telescope.

### 3.2 Trigger rates

*Rate versus pointing altitude:* The pointing altitude that optimizes Cherenkov light collection for 20 GeV gamma-ray showers is approximately 13 km above the Themis site. Hadron showers are harder to model, and a measurement of the hadron shower trigger rate as a function of pointing altitude is useful to choose the pointing strategy that will optimize the gamma/hadron signal-to-noise ratio. Figure 10 summarizes our measurements. In this particular study the multiplicity was 6 heliostats out of 6 above threshold. The numbers correspond to the charge of the H, He, and Li nuclei that we simulated. The sum of the three is shown by the circles. The absolute rate observed in the data (triangles) agrees well with the Monte Carlo prediction.

*Rates versus trigger threshold:*

Figure 11 shows the counting rate as a function of threshold as measured using a prototype of the hybrid analog/digital trigger built for the 40-heliostat experiment. The pointing altitude is 10 km above the site. A discriminator threshold is applied to the analog sum of phototube outputs within a subgroup, and the coincidence rate for two such sums is shown with the circles (corresponding to a sum of three outputs) and squares (sum of two outputs), using a 20 ns gate. The threshold in figure 11 is normalized to the number of phototubes in the sum (i.e. the threshold is divided by the number of channels combined in the discriminated analogic sum). The gain used to convert from millivolts to photoelectrons is the average of the gains of the channels in the sum. The solid line through the data is the sum of a power law fitted to the Cherenkov light from air showers, and a simulation of the night sky noise.

Both contributions are well described in terms of known quantities. The night sky light dominates below the 5 photoelectron threshold, and the solid line in this part is the trigger simulation for a photon flux of  $b = 0.6\gamma_e/\text{ns}$  (which is slightly above the measurement of section 2.5). Phototube afterpulsing is taken into account in the trigger simulation. We tested that coincidences at thresholds below the break point are due mainly to accidental overlap of random night sky photons by increasing the 20 ns discriminator output to 40 ns, and we verified that the observed rate at fixed threshold doubled, as expected

for accidentals. Changing the coincidence of a sum of two heliostats to a sum of three heliostats affects significantly the night sky light induced rate, as shown by the open markers in figures 11 and 12, but not the air shower part.

Above the 5 photoelectron breakpoint, the  $3 \oplus 3$  and  $2 \oplus 2$  data lie on a curve of the form  $f_C(s) = 40s^{-1.3}$  predominately due to Cherenkov flashes, where  $s$  is the threshold in photoelectrons/heliostat. The power law index of the integral rate curve is less than the index of 1.78 inferred from equation 2 which is reproduced by the Monte Carlo as shown in figure 12. and is due mainly to the fact that the Cherenkov yield of a hadron shower, normalized to the primary particle energy, is decreasing in our energy range. The rates in figure 12 are absolute: no *a posteriori* normalization was performed.

*Extrapolation to the full-scale experiment:* The agreement between the simulated night sky light counting rate and the experimental data allows us to estimate with good confidence the expected counting rate for a larger setup such as four groups of 9 heliostats (solid line number 1 in figure 11) or three groups of 6 heliostats (solid line number 2). The power law above a two photoelectron threshold is the result of a detailed Monte Carlo of the full-scale experiment. The dotted line (number 3) is an extrapolation of the measured  $3 \oplus 3$  proton trigger rate to the full-scale experiment, using mainly the fact that the field-of-view will be different. The simulated counting rate of the full-scale experiment is lower than the extrapolated counting rate. This is due to the fact that a third group of heliostats in the trigger requires a more uniform light pool, thus improving hadron rejection at the trigger level.

One of the conclusions of figure 11 is that a trigger threshold of about two photoelectrons, with an acceptable raw trigger rate is realistic for the full-scale experiment. This threshold should provide a gamma-ray energy threshold of about 20 GeV.

*Muon rates:* Muons falling near a group of heliostats are not detected because the light is not emitted in the volume defined by the intersection of the field-of-view of the two groups. We generated  $10^6$  muons above 10 GeV according to the measurements of [19], corresponding roughly to 75 minutes of exposure. Ten muon events triggered for a simulated pointing altitude of 6 km, from which we deduce that the muon rate is less than 4 mHz at the 95% confidence level. The 6 km altitude is probably due to the fact that the angle between the two field-of-views of the two groups of heliostats then corresponds to the altitude dependent Cherenkov angle.

### 3.3 Photoelectron distributions and energy thresholds

Figure 13 compares the differential photoelectron distribution with the prediction of the Monte Carlo simulation, for 15000 events recorded at a pointing altitude of 10 km. 6491 events remain after selection cuts. The digitized charge of all channels are combined to build the experimental differential photoelectron distribution. The predicted and measured rates are absolute. As stated before, a charge threshold of 7 photoelectrons on each channel and a requirement of 5 heliostats out of 6 above threshold was applied in the data analysis as well as in the Monte Carlo. The 90% point on the leading edge of the differential plot is at 6 photoelectrons, in good agreement with the trigger and analysis thresholds.

Figures 12 and 13 demonstrate the reliability of our detector simulation: our modeling of the detector response to atmospheric Cherenkov light reproduces our observations faithfully. The simulations correctly reproduce various parameters and distributions obtained from the experiment. We can therefore use our simulation to address further questions with confidence.

*Hadrons:* Figure 14 shows the Monte Carlo differential energy distribution for the proton triggers of the simulated histogram in figure 13. The energy threshold is near 300 GeV. The hybrid trigger provides a comparable but slightly lower threshold. The acceptance in the inset to figure 14 is in units of  $cm^2 sr$ .

*Gamma-rays:* Simulation of gamma-ray events in the same experimental conditions yields a gamma-ray threshold of 80 GeV. In the 40-heliostat experiment the Cherenkov light collection efficiency will be better, due to improved secondary mirrors and Winston cones. The gamma-ray energy threshold will thus be lower than that suggested by a naive extrapolation based on the curves in figure 11.

## 4 CONSEQUENCES FOR FUTURE LOW ENERGY ATMOSPHERIC CHERENKOV TELESCOPES

Two different approaches to ground-based detection of 20 to 200 GeV gamma-ray detection are being worked on. The MAGIC project aims to extend the imaging technique below the current minimum of about 200 GeV through greatly improved Cherenkov light collection [18], using a 17 m diameter mirror. They are developing a camera that would have over 50% quantum efficiency. The other approach is the sampling technique of STACEE [12] and CELESTE, which both rely on existing solar plants. The design of a full-scale instru-

ment sensitive in the 20 to 200 GeV range must wait for the results of these projects. Even so, the results presented in this paper allow us to underscore some elements of the choice between a sampler and an imager.

#### *4.1 Trigger level background rejection*

The Crab detections by Themistocle [7] and ASGAT [8] established the validity of wavefront sampling with a multi-telescope array. Sampling is less efficient than the imaging technique in the TeV domain: the angular precision is similar, but hadron rejection is worse. At lower energies the situation changes. The Cherenkov light yield for hadron showers below 100 GeV decreases faster than the energy, so that false triggers for imaging devices will be due mostly to muons falling at distances up to several mirror radii. A sampler triggers on simultaneous signals from distant telescopes. This trigger selects showers with a uniform light pool, such as gamma-ray showers or hadron showers that have fragmented mainly to a neutral pion. In particular, muons do not trigger the device.

Therefore an important result of the present study is the low trigger rate obtained at low energy threshold, as for example in figure 11. Extrapolation to the 40-heliostat array predicts about 20 Hz for a fraction of a Hz of gamma events from the Crab. The large imager project MAGIC expects a raw trigger rate of order 1 kHz for the same energy range. This high rate may be reduced by online and offline data reduction [18]. This will be better understood when data are available. At present, we can only speculate about how a sampling array might look.

#### *4.2 Towards a major low energy atmospheric Cherenkov detector*

The solar arrays permit low-cost full-scale testing of the sampling approach at low energy. Phototubes on each mirror as for Themistocle or ASGAT is better. The disadvantages of the solar tower set-up are:

- the incident angle of the Cherenkov light on the heliostats varies widely while tracking a cosmic source. A large incidence angle degrades the effective collection area and the light collection efficiency decreases with the increasing aberration effects. Conventional telescopes look straight at the shower while tracking the cosmic source and always work near their optical axis;
- the field-of-view must be less than 1 degree because of the limited space at the top of the tower. The small *fov* is exploited to increase the signal-to-noise (Cherenkov to night sky light) ratio, by pointing the heliostats at the

shower core (see section 3). This strategy limits the collection area to about  $2 \times 10^4 \text{ m}^2$  depending on the field-of-view. This shortcoming can be solved with conventional telescopes by using a camera with several pixels: a central phototube can provide trigger information, while a ring of phototubes would measure the centering. A similar arrangement is not possible at the top of a solar tower because of the lack of space.

In short, a sampling array of about the same size as CELESTE, for example, fifty telescopes of seven-meter diameter, each could exploit the sampling scheme without the drawbacks of a fixed central focus point. Energy threshold and overall performance could be directly extrapolated from CELESTE's. This extension of the solar plant test bench to an optimized sampling array - on an optimal site - might be the best towards a major low energy atmospheric Cherenkov detector. A clear consequence of the present study is that such a scheme is at least feasible.

## 5 CONCLUSIONS

We have used a solar array to detect Cherenkov light from air showers. We accurately measure the shower light emitted in the small volume at the intersection of the fields-of-view of two groups of three heliostats each.

Triggering on widely spaced heliostat groups has been shown to give good hadron and muon rejection.

The minimum trigger threshold at which the Cherenkov signal dominated the night sky background was 5 photoelectrons per heliostat. In our analysis the threshold was 7 photoelectrons, which corresponds to a hadron shower energy slightly above 300 GeV, or to a gamma-ray energy of 80 GeV. At this threshold the trigger rate was 6 Hz. We expect a threshold of 2 – 3 photoelectrons and a rate of 20 Hz with the optics now being installed, corresponding to a gamma-ray energy threshold below 30 GeV.

Our test results, and in particular the low trigger rate, confirm that wavefront sampling is an alternative to imaging as a basis for a high-performance gamma-ray detector in the 20 to 200 GeV energy range. We are presently commissioning a full-scale device which we expect to provide the first ground-based detection of cosmic gamma-rays in this energy range. The ongoing observations could establish that, even independently of existing solar arrays, wavefront sampling might be the best way to access an unexplored spectral window known to be particularly rich in astrophysical information.

## ACKNOWLEDGEMENTS

We gratefully acknowledge the contributions of the technical staffs of our laboratories and the IMP (CNRS) at Odeillo. Drs. Philippe Roy and Louis Behr play key roles in the continued progress of the project. We thank Electricité de France for allowing use of the Themis site. Funding was provided by the Institut National de Physique des Particules et de Physique Nucléaire of the Centre National de Recherche Scientifique; the Grant Agency of the Czech Republic; by the University of Bordeaux; by the Ecole Polytechnique; and by the Regional Councils of Aquitaine and of Languedoc-Roussillon.

## References

- [1] CELESTE experimental proposal. See <http://wwwcenbg.in2p3.fr/Astroparticule> or contact the author.
- [2] C. von Montigny *et al*, *Ap. J.* **440** (1995) 525.
- [3] D.J. Thompson *et al*, *Ap. J.* **465** (1996) 385.
- [4] O.C. De Jager, F.W. Stecker, & M.H. Salamon, *Nature* **369** (1994) 294.
- [5] T.C. Weekes, *Phys. Rep.* **160** (1988).
- [6] J. Quinn *et al*, *Ap. J. Lett.* **456** (1996) 83.
- [7] P. Baillon *et al*, *Astropart. Phy.* **1** (1993) 341.
- [8] P. Goret *et al*, *A&A* **270** (1993) 401.
- [9] R.J. Protheroe *et al* in *it Highlights of the XXV<sup>th</sup> Int. Cosmic Ray Conf.*, Durban (1997).
- [10] D.J. Thompson *et al*, *Ap.J.S.* **101** (1995) 259.
- [11] Mini-circuits PSC-3-1W, P.O. Box 350166, New York 11235-0003.
- [12] M.C. Chantell *et al*, *EFI preprint 38-97* (accepted by NIM).  
R. Ong *et al*, *Astropart. Phys.* **5** (1996) 353.
- [13] R. Mirzoyan and E. Lorenz, *proc. "Towards a Large Atmospheric Čerenkov Detector-IV"*, Padova 1995.
- [14] M. Kertzmann and G. Sembronski, *Nucl. Instr. Meth.* **343A** (1994) pp.629-643.
- [15] J.N. Capdevielle *et al* Karlsruhe KfK report 4998 (1992).
- [16] Masakatsu Ichimura *et al*, *Phys. Rev.* **48D** (1993) 1949.
- [17] B. Wiebel-Sooth, P. Biermann, and H. Mayer, *accepted by A&A*. Preprint astro-ph/9709253.

- [18] R. Mirzoyan, E. Lorenz, and Gonzáles, *proc. "Towards a Large Atmospheric Čerenkov Detector-IV"*, Durban 1997.
- [19] R. Bellotti *et al*, *Phys. Rev.* **53D** (1996) 35.



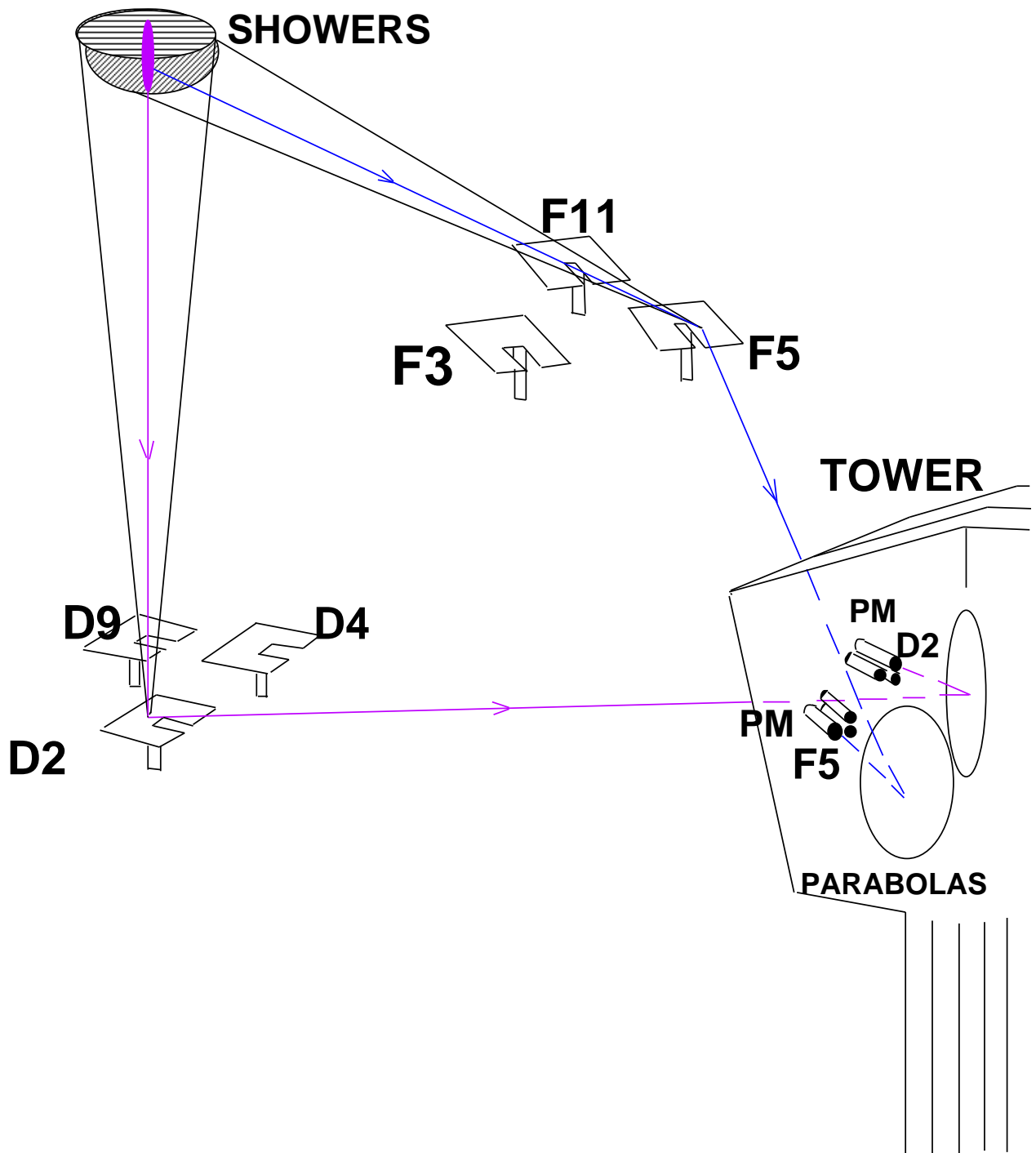


Fig. 1. Principle of a “solar farm” Cherenkov gamma-ray telescope, showing the six heliostats and the two searchlight mirrors used during tests at Themis in the Winter of 1996/1997. Heliostats and secondary mirrors are not to scale. The tower is 100 meters tall.

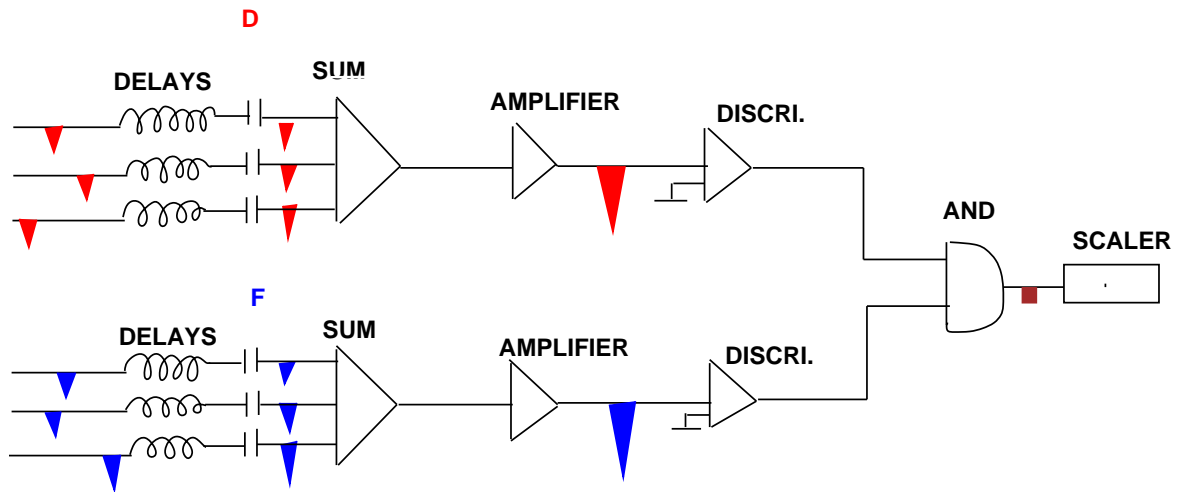


Fig. 2. Hybrid analog-digital trigger layout for the six-heliostat array.

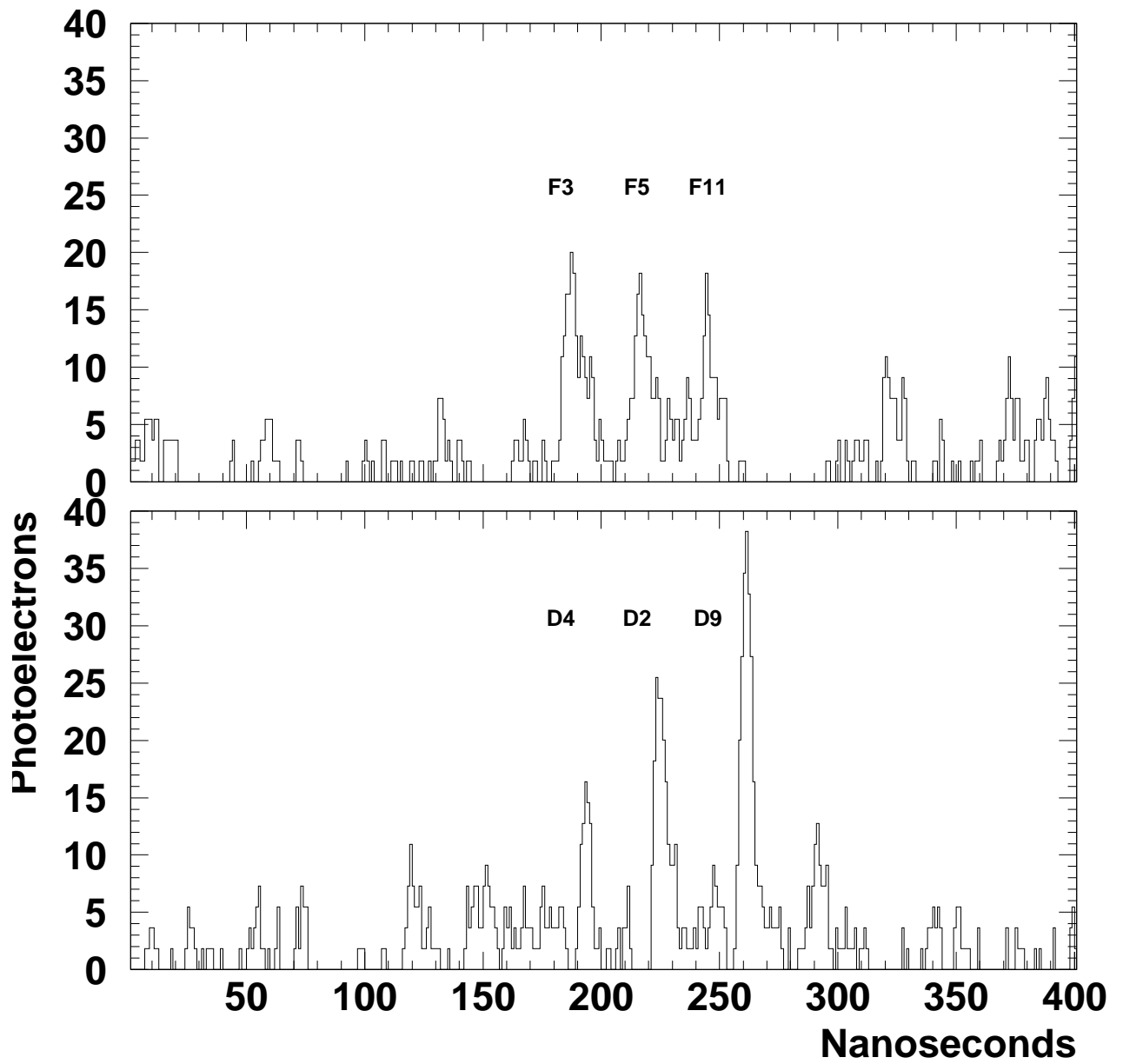


Fig. 3. Typical Cherenkov flash as seen by the six phototubes and recorded by two Flash ADC circuits. The labels are the heliostat names shown in figure 1.

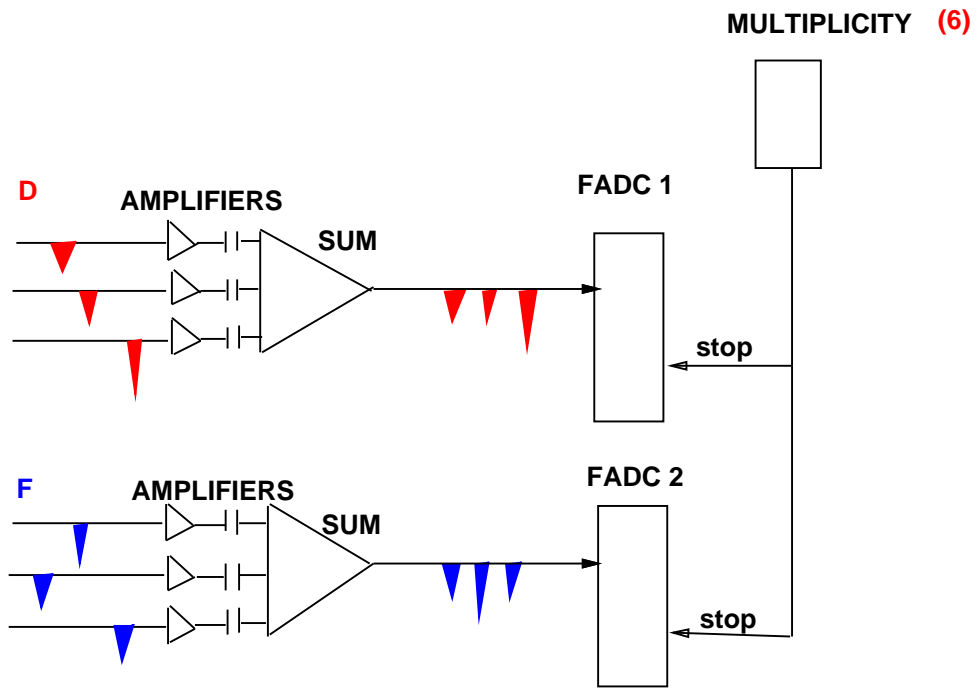


Fig. 4. Scheme whereby six photomultiplier signals are digitized using two Flash ADC channels.

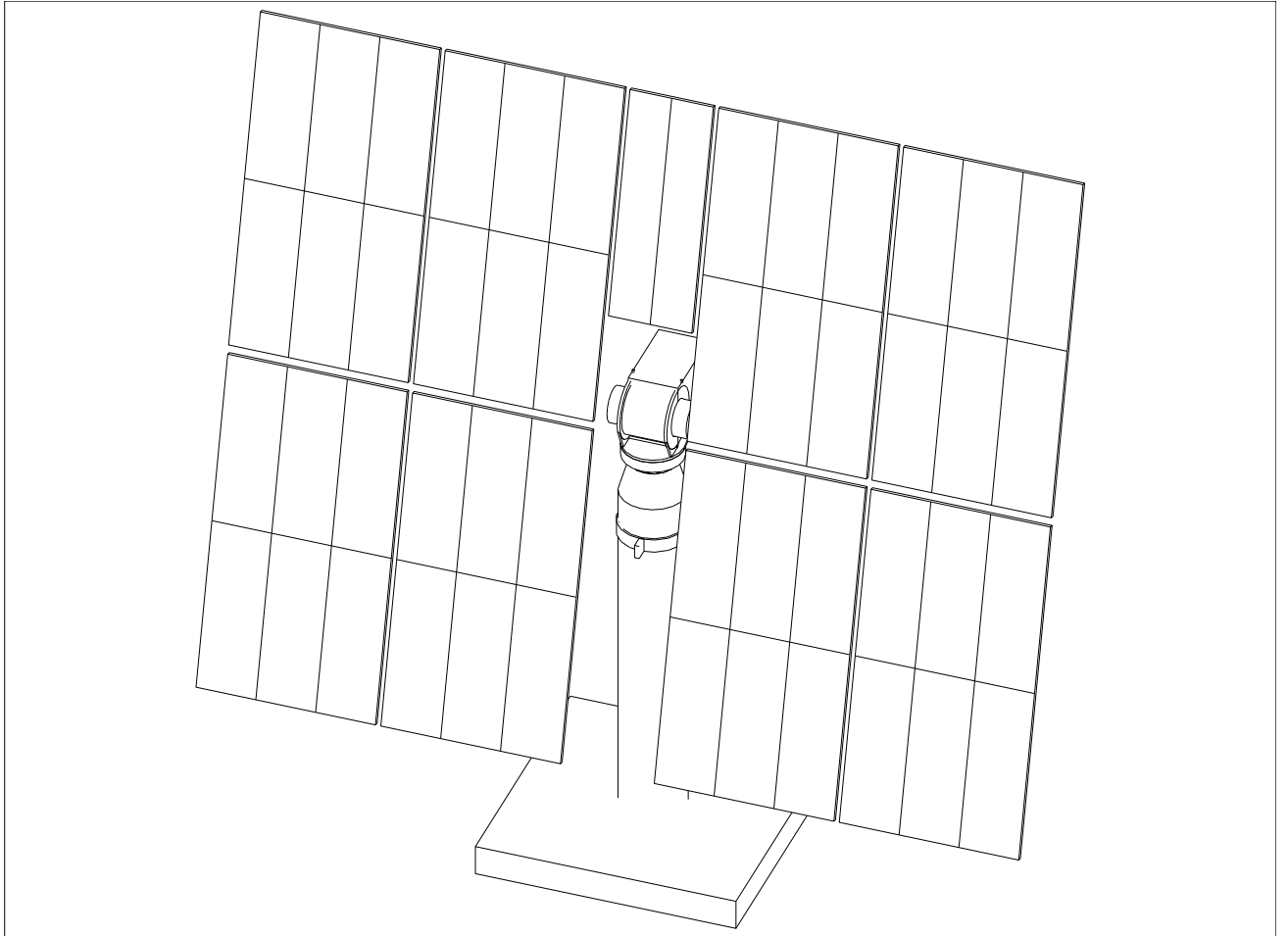


Fig. 5. A single Thémis heliostat mirror (7.3 by 8.8 meters) on its alt-azimuth mounting.

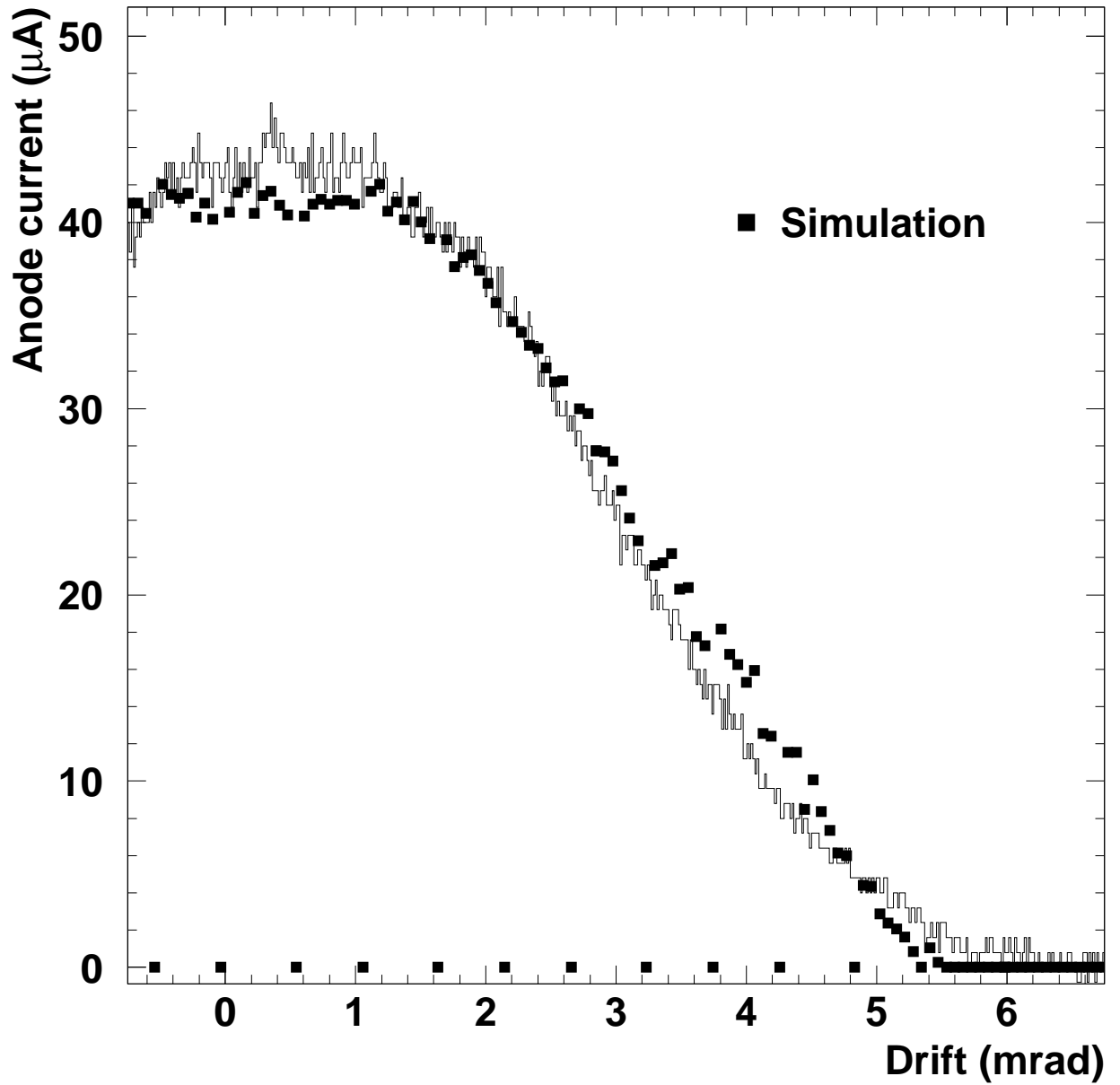


Fig. 6. Drift scan of the star  $\alpha\text{Leo}$ . Data: measured phototube current. Simulation: ray tracing calculation of the heliostat-parabola combination.

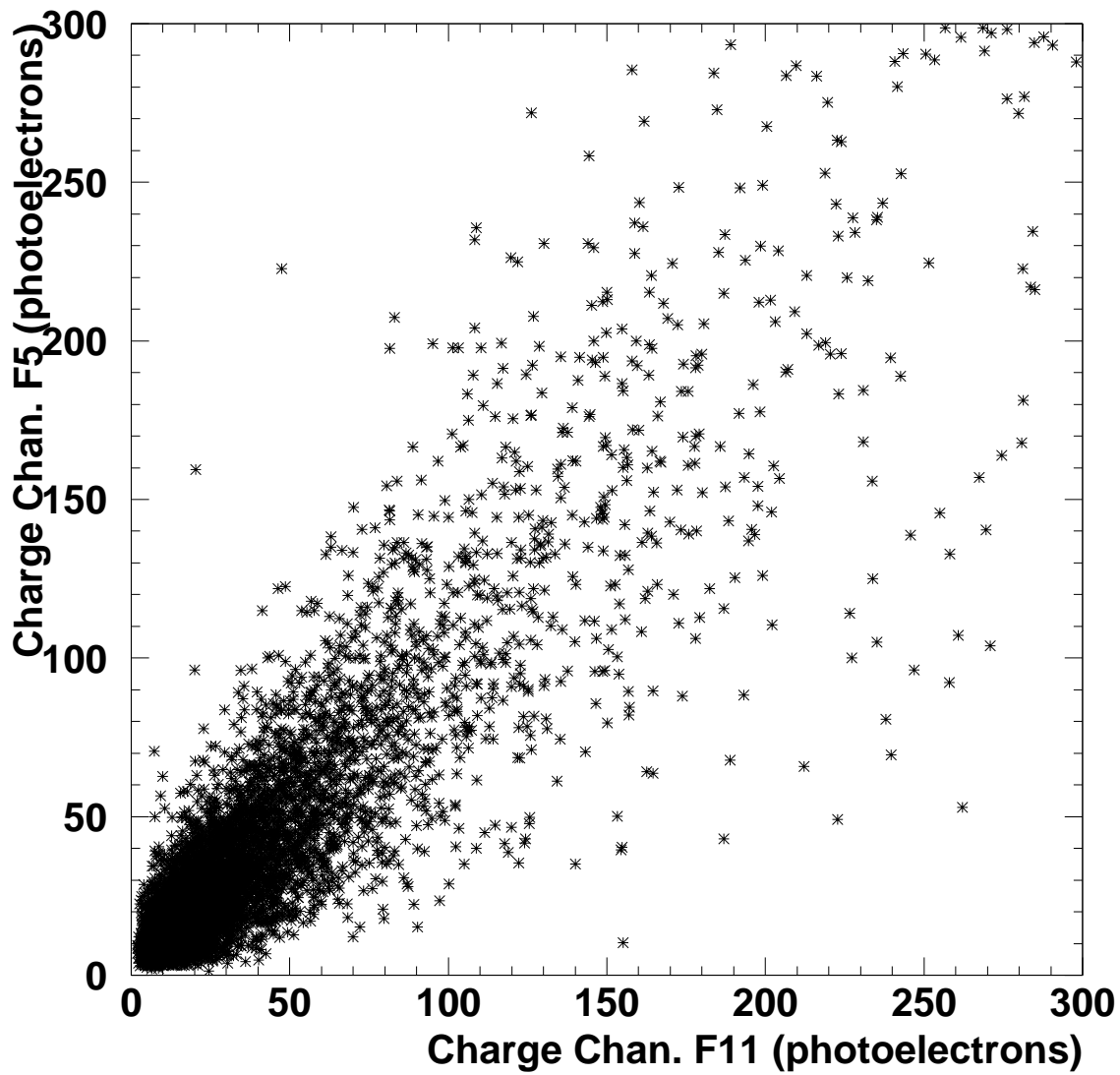


Fig. 7. Phototube pulseheight in heliostat F5 versus the pulseheight in heliostat F11, for six-fold trigger coincidences while pointing at 10 km, recorded using the Flash ADC's.

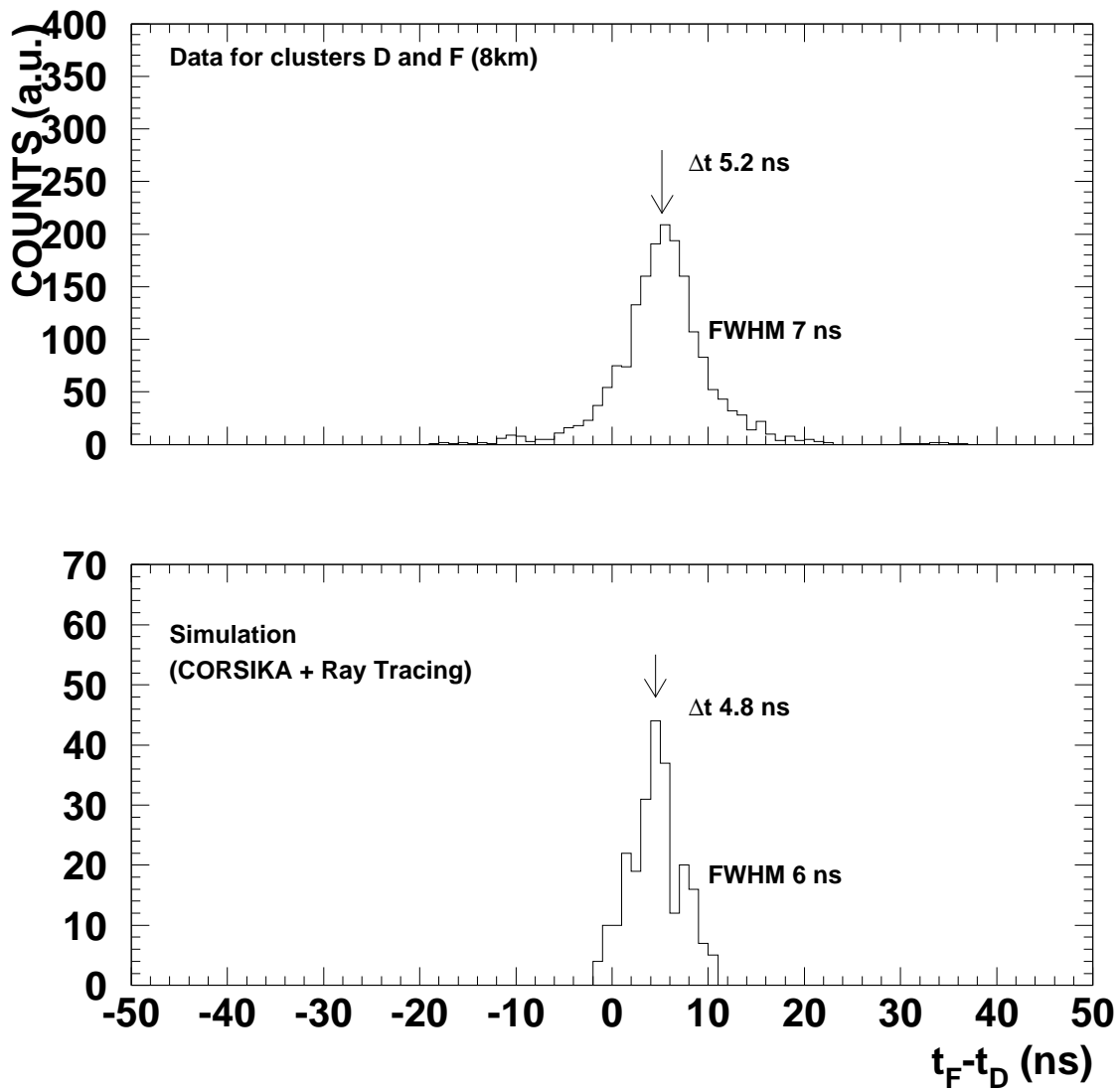


Fig. 8. Difference of the average arrival time of the Cherenkov pulse on the F and D heliostats, when pointing at 8 km above heliostat D2. Top: data. Bottom: Corsika Monte Carlo simulation.



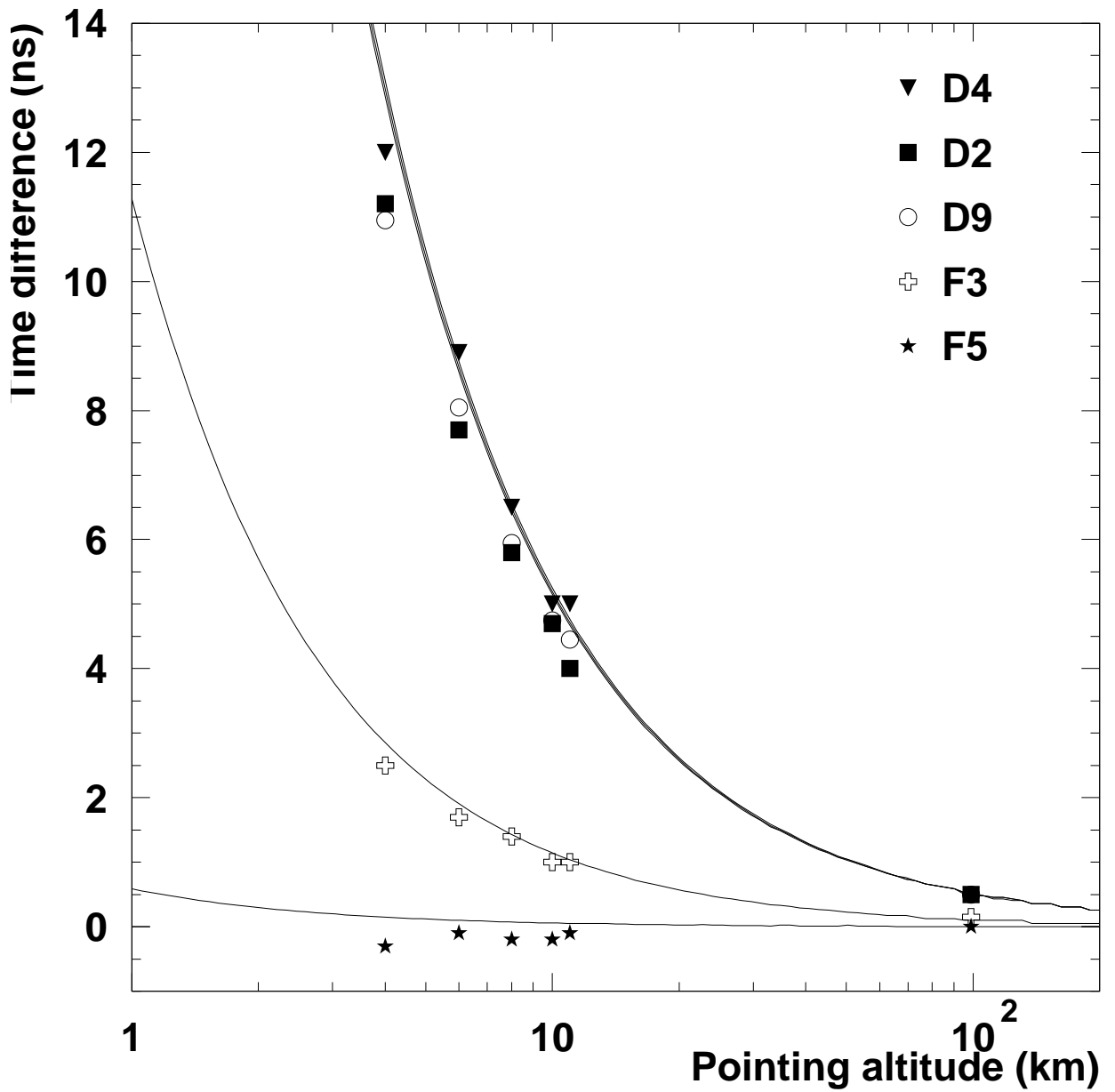


Fig. 9. Cherenkov pulse arrival times with respect to F11, as a function of pointing altitude (above the site), for different heliostats.

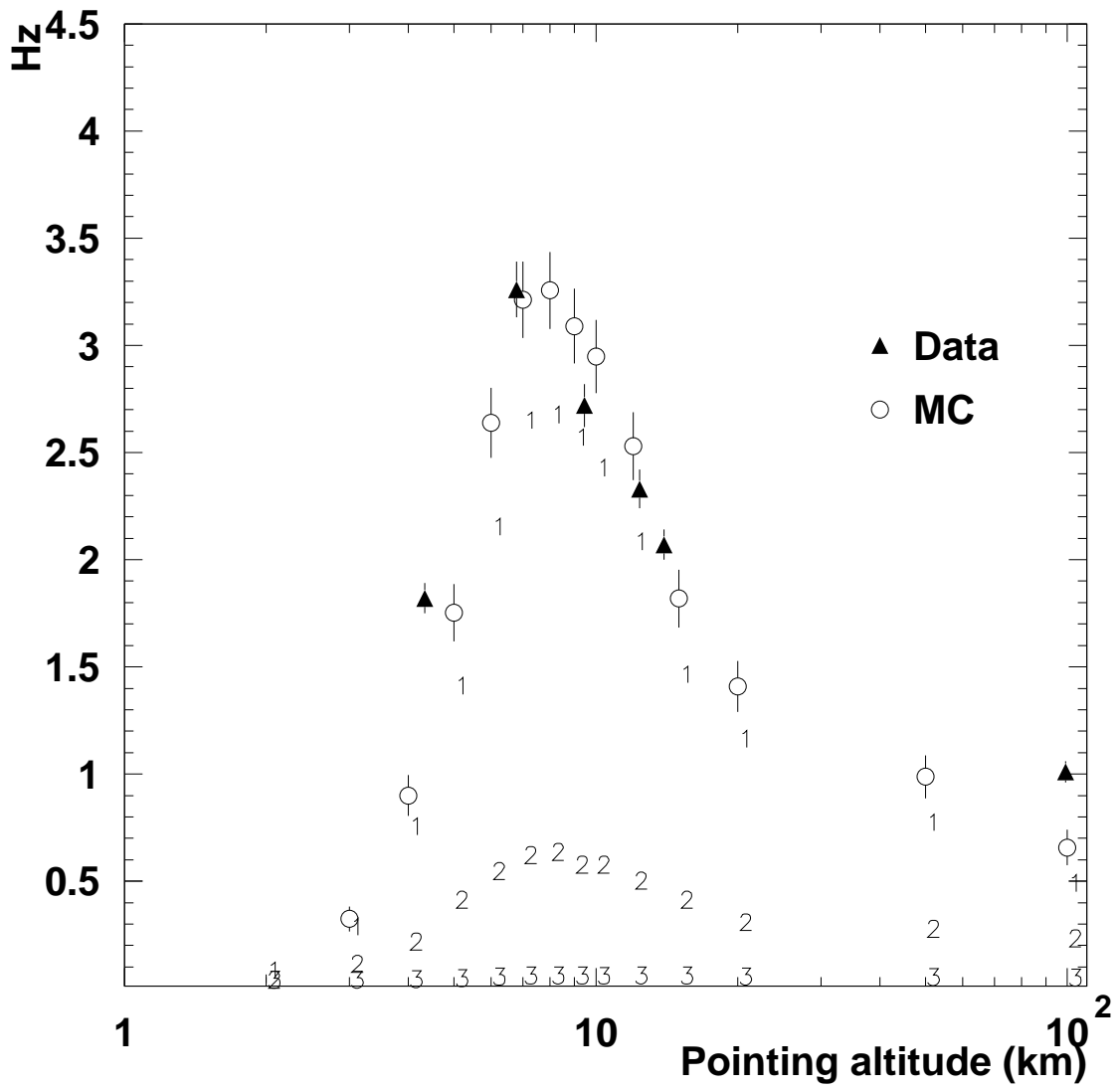


Fig. 10. Counting rate versus pointing altitude above the detector after data analysis cuts. Triangles: Data. Circles: sum of the Monte Carlo H (1), He (2), and Li (3) contributions.

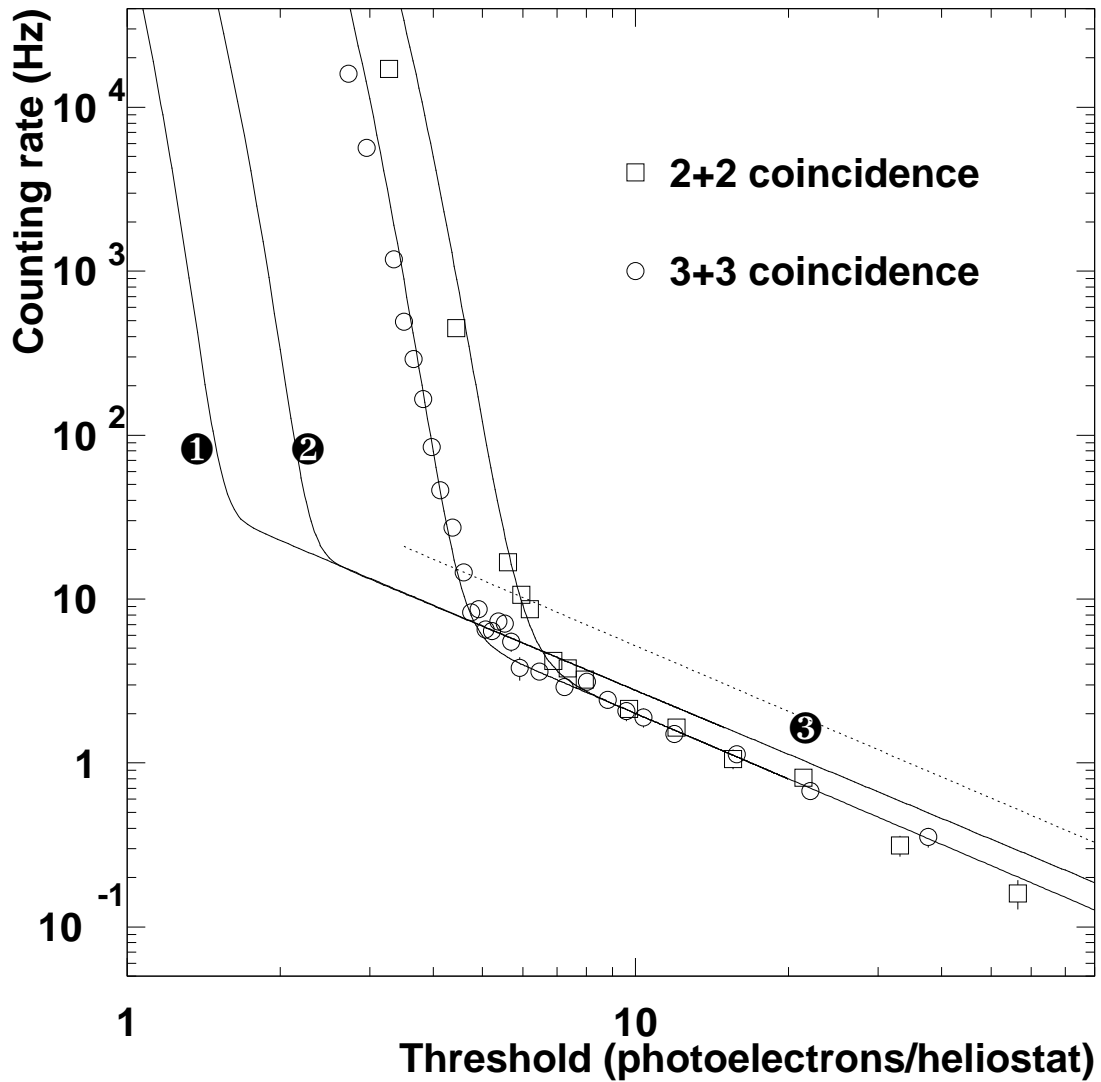


Fig. 11. Counting rate versus trigger threshold using a coincidence of two analog sums. Circles: Coincidence of two sums of three phototubes. Squares: Coincidence of two sums of two phototubes. Curve number 1 (2): expected rates for respectively 3 (4) groups of 6 (9) heliostats. See the text for the improved level of dotted line 3.

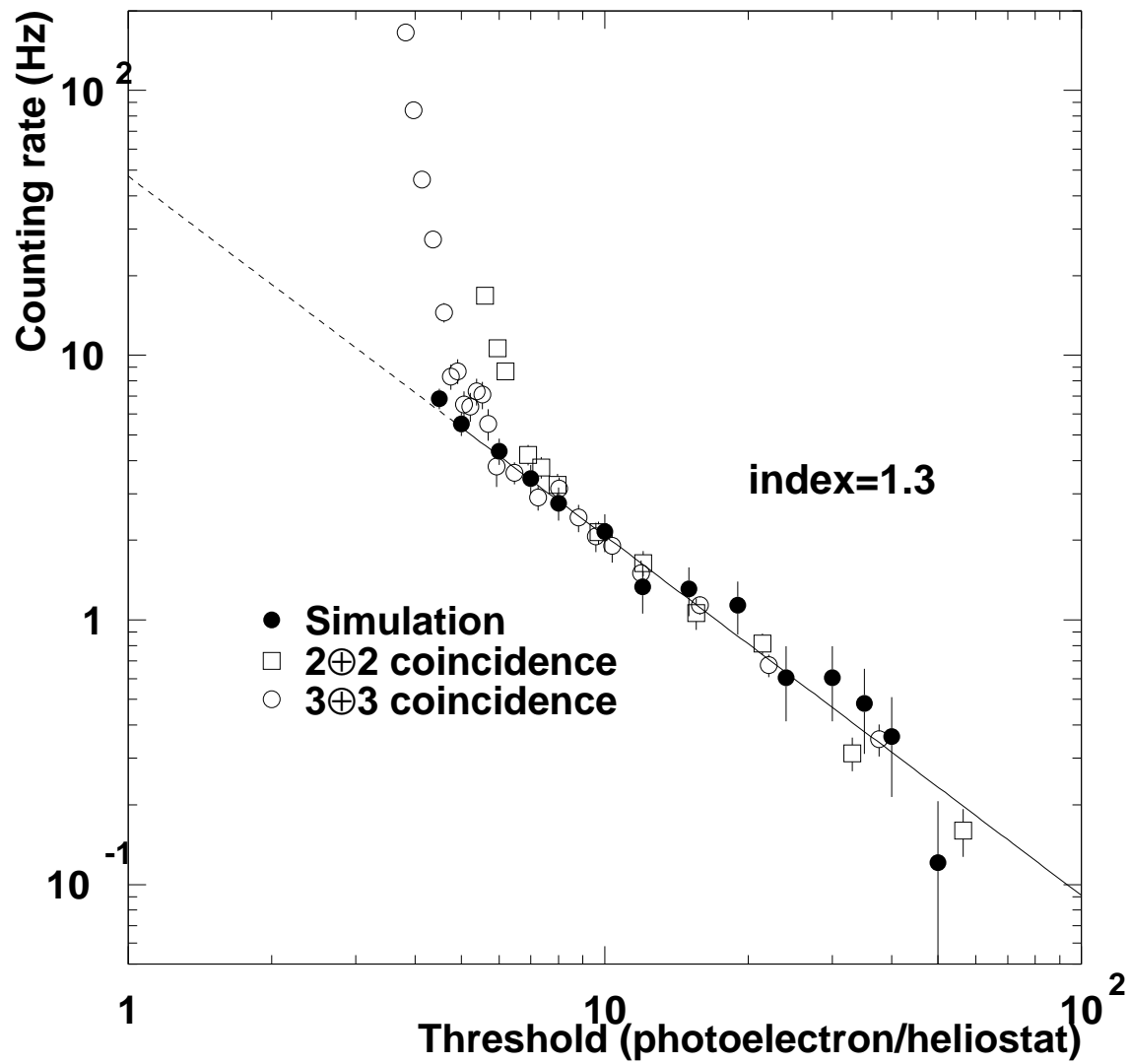


Fig. 12. Comparison of Monte Carlo and measured counting rates versus trigger threshold for the coincidence of two analog sums. Open: Data. Solid: Air shower simulation.

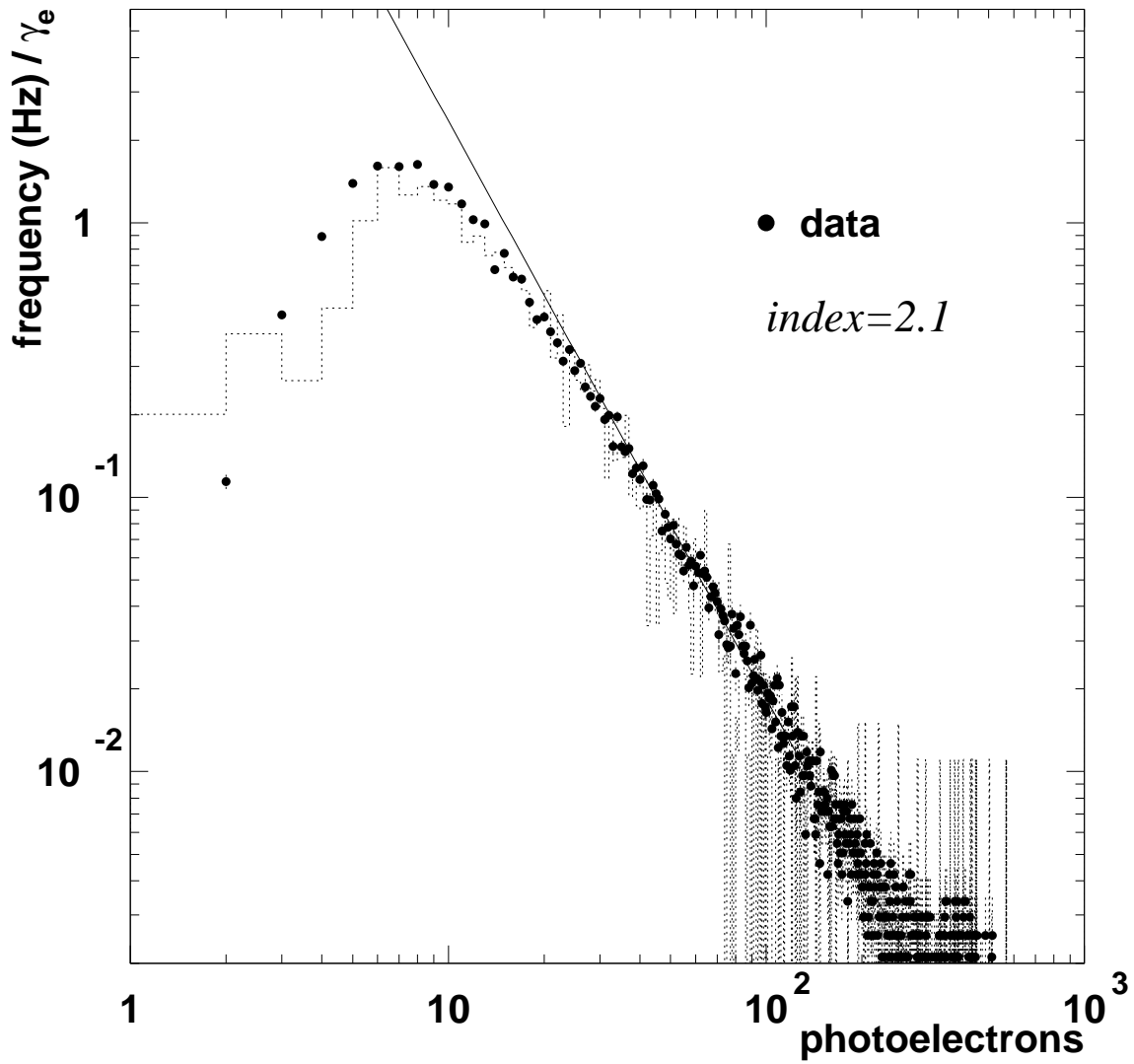


Fig. 13. Differential charge distribution of all channels expressed in photoelectrons, while pointing at 10 km above the site. The histogram is the Monte Carlo prediction.

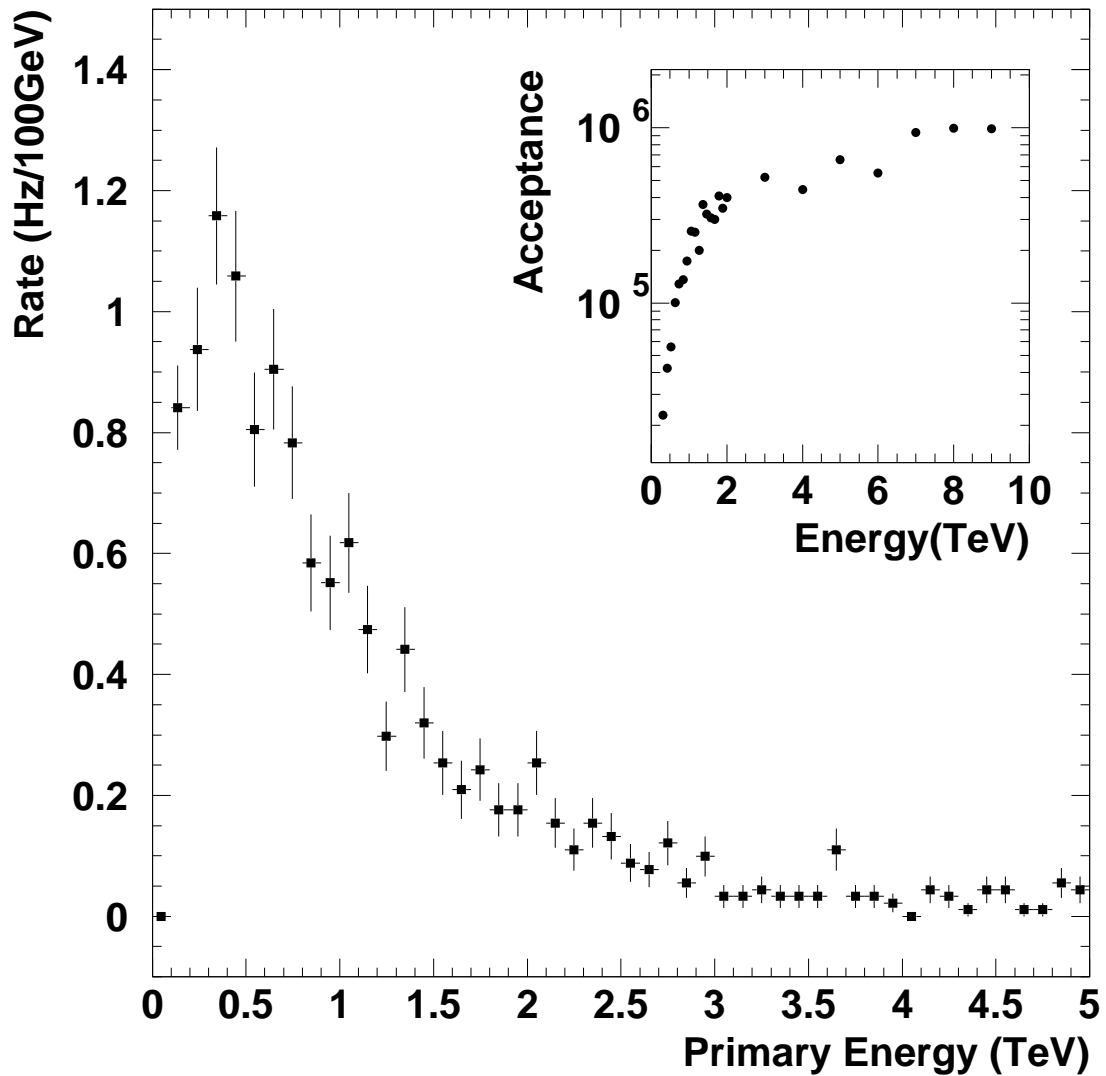


Fig. 14. Monte Carlo differential rate of reconstructed showers as a function of primary proton energy, for a pointing altitude 10 km above the site and normalized to the input spectrum. The single channel threshold is 7 photoelectrons. The energy threshold is near 300 GeV. Inset: the acceptance in units of  $cm^2sr$ .